



1    **The precipitation variability of wet and dry season at the interannual**  
2    **and interdecadal scales over eastern China (1901–2016): The impacts**  
3    **of the Pacific Ocean**

4    Tao Gao<sup>1,4,5</sup>, Fuqiang Cao<sup>2,3\*</sup>, Li Dan<sup>3</sup>, Ming Li<sup>2</sup>, Xiang Gong<sup>5</sup>, and Junjie Zhan<sup>6</sup>

5        <sup>1</sup> State Key Laboratory of Numerical Modeling for Atmospheric Sciences and  
6    Geophysical Fluid Dynamics, Institute of Atmospheric Physics, Chinese Academy of  
7    Sciences, Beijing 100029, China

8        <sup>2</sup> School of geosciences, Shanxi Normal University, Linfen 041000, China

9        <sup>3</sup> CAS Key Laboratory of Regional Climate-Environment Research for Temperate  
10   East Asia, Institute of Atmospheric Physics, Chinese Academy of Sciences, Beijing,  
11   China

12        <sup>4</sup> College of Urban Construction, Heze University, Heze 274000, China

13        <sup>5</sup> School of Mathematics and Physics, Qingdao University of Science and Technology,  
14   Qingdao 266061, China

15        <sup>6</sup> Shunyi Meteorological Service, Beijing, 101300, China

16  
17    \*Corresponding author address: Dr. Fuqiang Cao, 1 Gongyuan Road, Linfen 041000,  
18    P. R. China.

19    Email: wq2006126@126.com

20

21



22 **Abstract:** The spatiotemporal variability of rainfall in dry (October- March) and wet  
23 (April-September) seasons over eastern China is examined based on gridded rainfall  
24 dataset from University of East Angela Climatic Research Unit during 1901–2016.  
25 Principal component analysis is employed to identify the dominant variability modes,  
26 wavelet coherence is utilized to investigate the spectral characteristics of leading  
27 modes of precipitation and their coherences with the large-scale modes of climate  
28 variability, and Bayesian dynamical linear model is adopted to quantify the  
29 time-varying correlations between climate variability modes and rainfall in dry and  
30 wet seasons. Results show that first and second principal components (PCs) account  
31 for 34.2% (16.1%) and 13.4% (13.9%) of variance in dry (wet) season, and their  
32 changes are roughly coincident with phase shifts of the El Niño-Southern Oscillation  
33 (ENSO) in both seasons. The anomalous moisture fluxes responsible for the  
34 occurrences of precipitation events in eastern China are asymmetry during high and  
35 light rainfall years in dry (wet) season. ENSO has a 4- to 8-year signal of the  
36 statistically positive (negative) association with rainfall during dry (wet) season in  
37 eastern China. The statistically significant positive (negative) associations between  
38 Pacific Decadal Oscillation (PDO) and precipitation are found with 9- to 15-year (4-  
39 to 7-year) signal. The impacts of PDO on rainfall in eastern China exhibit multiple  
40 time scales as compared to ENSO episodes, while PDO triggers a stronger effect on  
41 precipitation in wet season than dry season. The interannual and interdecadal  
42 variations in rainfall over eastern China are substantially modulated by drivers  
43 originated from Pacific Ocean, the finding has meaningful implications for regional  
44 hydrologic predictability and water resources management.

45

46 **Keywords:** Precipitation over eastern China; Principal component analysis; Wavelet  
47 spectral analysis; Bayesian dynamical linear model

48



## 49 1. Introduction

50 As a densely populated area with lots of industrial and agricultural activities, eastern  
51 China is frequently affected by the catastrophic floods and droughts derived from  
52 variability of precipitation events (Liu et al., 2015; Huang et al., 2017; Yang et al.,  
53 2017; Luo and Lau, 2018; Ge et al., 2019). For example, intense rainfall in southern  
54 China resulted in disastrous floods over the lower reach of Yangtze River basin (YRB)  
55 in 1991, 1996, 1998 and 1999. Seriously deficient precipitation in northern China  
56 caused a severe drought of 226 days without stream discharge over the Yellow River  
57 basin (Qian and Zhou, 2014; Xu et al., 2015; Zhang and Zhou, 2015). It is therefore of  
58 great importance to investigate the rainfall variability in eastern China and its  
59 associated physical mechanisms.

60 Many studies pointed out that the variations in rainfall in eastern China are strongly  
61 influenced by East Asian monsoon, which is closely related to the sea surface  
62 temperature (SST) anomalies over the Pacific Ocean (Wang and Zhou, 2005; Huang  
63 et al., 2017; Yang et al., 2017). At the interannual scale, heavy rainfall events often  
64 occur over southern China during El Niño episodes (e.g., Zhang et al., 1996; Wang et  
65 al., 2000; He et al., 2017). At the interdecadal scale, the variations in precipitation  
66 events over eastern China are remarkably impacted by tropical Pacific SST and  
67 western Pacific subtropical high (WPSH, Chang et al., 2000a; Zhu et al., 2011; Li et  
68 al., 2019). Moreover, SST anomalies over the tropical Indian Ocean and tropical  
69 eastern Pacific also account for the shifts of the positive-negative-positive rainfall  
70 patterns over eastern China via their influences on WPSH (Chang et al., 2000b; Hu et



71 al., 2018). Thus, a better understanding of interannual and interdecadal changes  
72 stemming from the variability of air-sea interaction over the Pacific Ocean is crucial  
73 to the interpretation for the variations in rainfall over eastern China.

74 The El Niño-Southern Oscillation (ENSO) is a strong air-sea coupled mode at the  
75 interannual scale over the tropics, it is also the important source of interannual  
76 variability of the global climate system (Webster et al., 1998). ENSO significantly  
77 impacts rainfall over eastern China by means of the atmospheric teleconnections (e.g.,  
78 Wang et al., 2008; Jin et al., 2016; Liu et al., 2016; Sun et al., 2017; Gao et al., 2017).  
79 Wang et al. (2000) proposed that the key system of Pacific-East Asian teleconnection  
80 responsible for linkages between ENSO and precipitation anomalies over eastern  
81 China is an anomalous low-level anticyclone located over the western North Pacific  
82 (WNP), this is induced by local air-sea interactions and large-scale equatorial heating  
83 anomalies. Wu et al. (2003) further argued that the similar positive correlation  
84 between springtime rainfall over the mid-lower reaches of YRB and ENSO is linked  
85 to the evolution of ENSO-related seasonal rainfall anomalies over East Asia.  
86 Moreover, the summertime rainfall over the YRB and to its south is expected to be  
87 strengthened (weakened) during El Niño (La Niña) years. Huang and Wu (1989)  
88 documented that the drought in northern and southern China as well as flood over  
89 central China are associated with the developing stage of warm ENSO events, and the  
90 reversed relationship is seen in decaying stage of the warm events. These patterns of  
91 rainfall in eastern China may also be related to strong convective activities in the  
92 Philippines, with the effects from western Pacific warm pool through shifting the



93 WPSH northward (Huang and Sun, 1992; Jin et al., 2016). The latest research  
94 suggested that the patterns of seasonal rainfall anomaly in eastern China are  
95 modulated by the different types of La Niña decay, these are attributed to the  
96 responses of large-scale circulation anomalies induced by different types of La Niña  
97 episodes (Chen et al., 2019).

98 At the interdecadal scale, northern China experienced dry and wet alternations,  
99 with above-normal rainfall around the 1950s and severe droughts around the 1970s  
100 and 1980s. While the YRB and southern China suffered apparent shifts of  
101 precipitation patterns in the 1970s and 1990s (Zhu et al., 2015). A growing body of  
102 studies indicated that these shifts of rainfall distribution over eastern China are caused  
103 by the changes in Pacific decadal oscillation (PDO) phases. Yang and Lau (2004)  
104 reported a close relationship between the positive PDO and decreasing trends of  
105 summertime rainfall events over eastern China. Based on surface wetness indices, Ma  
106 (2007) further pointed out an anti-correlation between rainfall in northern China and  
107 PDO phases, suggesting more droughts over northern China during positive phase of  
108 PDO, and vice versa. The strengthened (weakened) precipitation over the Huang-Huai  
109 (Yangtze) River basin from 2000 to 2008 compared to those during 1979-1999 is  
110 triggered by the transition from warm to cold phase of the PDO around the 2000s,  
111 which is attributed to the weakened westerly winds and warming over the Lake Baikal  
112 induced by negative PDO after 2000s (Zhu et al., 2011). The possible modulation of  
113 the PDO on the East Asian summer monsoon (EASM) and East Asian winter  
114 monsoon (EAWM), which are associated with summer and winter rainfall changes in



115 eastern China, respectively, has also documented in previous studies (e.g., Yu, 2013;  
116 Chen et al., 2013). Zhou et al. (2013) pointed out an anti-correlation between the PDO  
117 and EASM since 1950s, and negative phases of the PDO correspond to a stronger  
118 EASM with more precipitation events over northern China. A much stronger EASM  
119 tends to appear after a weak EAWM in positive phases of the PDO than that in  
120 negative phases of the PDO (Chen et al., 2013). Existing studies also reported the  
121 similar relationship between positive phase of the PDO and drier conditions in  
122 northern China, and revealed that a warm phase of PDO in the 1976/1977 resulted in a  
123 weakened EASM associated with aridity over northern China in the 1980s and 1990s  
124 (Qian and Zhou, 2014; Zhu et al., 2015; Yang et al., 2017; Gao and Wang, 2017).  
125 Furthermore, the relationship between interdecadal variability of rainfall patterns over  
126 eastern China and phase transitions of PDO is also identified and verified by coupled  
127 climate model simulations (e.g., Li et al., 2010; Yu et al., 2015).

128 The above analyses show that most previous studies focused on the impacts of  
129 ENSO and PDO on the variations in seasonal rainfall over eastern China. However,  
130 the main rainy season in China, particularly in eastern China, does not follow  
131 climatological seasonal boundaries. Usage of boreal standard seasons may therefore  
132 unavoidably break the natural rainy distribution at the temporal scale, affecting the  
133 robustness of the analytical results (Zhai et al., 2005). Up to now, the issue on whether  
134 the ENSO and PDO can contribute to the interannual and interdecadal rainfall  
135 variability in major rainy seasons over eastern China is still unclear. In this study, we  
136 utilize April–September as the wet half year (wet season) and October–March as the



dry half year (dry season), respectively, to examine the effects of ENSO and PDO on the precipitation variability at the space-time scale, since the rainfall in eastern China is principally concentrated during April–September (Bao 1987; Domroes and Peng 1988; Zhai et al., 2005). Data and methods are described in section 2. The results are provided in section 3. Section 4 presents the discussion and conclusions.

## 2. Data and Methods

### 2.1 Data

A dataset of daily accumulated rainfall amount at 756 meteorological stations during 1960-2015 across China is employed in this study. This dataset is developed at Climate Data Center of the National Meteorological Center of the China Meteorological Administration (<http://cdc.cma.gov.cn/dataSetDetailed.do>), including almost all the first and second class national climatological stations. The accurate quality control procedures are conducted to check the temporal inhomogeneity and missing values, and screen the related stations in the following analyses, meaning that the stations having too many missing rainfall values are dropped. For example, a year is considered as the missing year if there exists more than 10% missing days, and a station with less than 5% missing years is retained. After these procedures, 436 stations meet these criteria and are retained in the subsequent analyses. Another rainfall dataset is a Global land monthly precipitation dataset from University of East Angela Climatic Research Unit (CRU), which has a high resolution of  $0.5^{\circ} \times 0.5^{\circ}$  over land from 1901 to 2016. The CRU data covers a longer period as compared to observed counterpart, therefore, it is more suitable for examining multi-decadal



159 variability. More information about this dataset is referred to Harris et al. (2014).

160 We select monthly global circulation variables from National Centers for  
161 Environmental Prediction/National Center for Atmospheric Research (NCEP/NCAR)  
162 Reanalysis data (Kalnay et al., 1996). SST data are obtained from the Hadley Centre,  
163 Met Office (Rayner et al., 2003). ENSO index is obtained from the Climate Prediction  
164 Center of NOAA  
165 ([http://origin.cpc.ncep.noaa.gov/products/analysis\\_monitoring/ensostuff/detrend.nino](http://origin.cpc.ncep.noaa.gov/products/analysis_monitoring/ensostuff/detrend.nino)  
166 [34.ascii.txt](http://origin.cpc.ncep.noaa.gov/products/analysis_monitoring/ensostuff/detrend.nino)). The PDO index is extracted from the Earth System Research Laboratory  
167 of NOAA (<http://www.esrl.noaa.gov/psd/data/correlation/pdo.data/>).

## 168 **2.2 Method**

### 169 **2.2.1 Principle component analysis**

170 The gridded CRU precipitation dataset is subjected to the principle component  
171 analysis (PCA), which is a widely utilized method to extract the dominant temporal  
172 and spatial modes of the variability based on mutually correlated dataset. The leading  
173 principal component (PC) explains the most of variance, with the second PC  
174 decreases thereafter. Moreover, the leading PCs can reduce dimension of the original  
175 dataset, because they capture the most of variance. The detailed description of the  
176 PCA refers to Hannachi et al. (2007). To identify the effects of climate variability  
177 modes on variations in rainfall over eastern China, the correlations between the  
178 leading PCs and climate variability modes are calculated to understand the  
179 telecommunications. The composited maps of the atmospheric variables are analyzed  
180 to examine the physical mechanisms responsible for the rainfall variability, based on



181 the high and light 25th percentile values of the daily rainfall in wet and dry seasons,  
 182 respectively.

### 183 2.2.2 Wavelet coherence

184 The wavelet coherence is a widely used technique, based on how coherent the  
 185 cross-wavelet transform is in time frequency space. It can preferably access the  
 186 detailed relationships between two time series with different time periods and  
 187 disparate frequency ranges (e.g., Grinsted et al., 2004; Coulibaly and Burn, 2005).  
 188 Given two particular time series  $x_n$  and  $y_n$ , the wavelet coherence of them can be  
 189 expressed as

$$190 \quad W^{XY} = W^X W^{Y*} \quad (1)$$

191 where  $*$  represents their complex conjugation. Correspondingly, the cross-wavelet  
 192 power can be expressed as  $|W^{XY}|$ . And complex argument  $\arg(W^{xy})$  is considered as  
 193 local relative phases between the time series  $x_n$  and  $y_n$ , which are applicative in both  
 194 frequency and time domains. The wavelet coherence of the time series can be defined  
 195 according to Torrence and Webster (1999).

$$196 \quad R_n^2(s) = \frac{|S(s^{-1}W_n^{XY}(s))|^2}{S(s^{-1}|W_n^X(s)|^2) \cdot S(s^{-1}|W_n^Y(s)|^2)} \quad (2)$$

197 where  $S$  is the smoothing operator, which is further written as,

$$198 \quad S_{time}(W) = S_{scale}(S_{time}(W_n(s))) \quad (3)$$

199 where  $S_{scale}$  and  $S_{time}$  denote the smoothing along wavelet scale axis and time,  
 200 respectively. It is natural to design the smoothing operator so that it has a similar  
 201 footprint as the wavelet.



202 The related codes for the wavelet coherence used in the present study can be freely  
 203 downloaded from <http://www.pol.ac.uk/home/research/waveletcoherence/>. The  
 204 wavelet coherence is used to examine the correlation between ENSO/PDO and  
 205 rainfall over eastern China.

### 206 **2.2.3 Bayesian dynamic linear model**

207 The increases in amplitude of the SST anomaly patterns over the Pacific Ocean in the  
 208 context of global warming trigger non-stationarity changes in regional rainfall (Wang  
 209 et al., 2013; Krishnaswamy et al., 2015; Rajagopalan and Zagana, 2016). The  
 210 Bayesian dynamic linear model (BDLM) is employed to analyze the non-stationarity  
 211 and epochal fluctuations between the climate variability modes and rainfall in eastern  
 212 China. The description of BDLM model as follows,

$$213 \quad \begin{cases} y_t = \alpha_t + x_t \beta_t + v_t, & v_t \sim N(0, V_t) \\ \alpha_t = \alpha_{t-1} + \omega_{\alpha,t}, & \omega_{\alpha,t} \sim N(0, W_{\alpha,t}) \\ \beta_t = \beta_{t-1} + \omega_{\beta,t}, & \omega_{\beta,t} \sim N(0, W_{\beta,t}) \end{cases} \quad (4)$$

214 where  $y_t$  is the leading PCs of rainfall over eastern China,  $x_t$  is the covariate  
 215 (climate variability modes, i.e., ENSO and PDO), and  $\alpha_t$  and  $\beta_t$  are the dynamic  
 216 intercept and slope coefficients at time  $t$ .  $\omega_t$  is the corresponding evaluation error  
 217 and  $W_t$  is the corresponding scalar greater than zero.

218 Unlike traditional linear regression methods that cannot characterize the  
 219 time-varying relationship, BDLM can model and understand the non-stationarity in  
 220 the relationships between large-scale modes of climate variability and regional  
 221 precipitation with time. This method has been used to model monsoonal precipitation  
 222 variability in India and China, and shows better performance and more interesting



insights than the traditional regression method (Krishnaswamy et al., 2015; Gao et al., 2017). For the BDLM, the regression coefficient varies with time compared to the traditional regression, in which the coefficient remains fixed.

### 3. Results

#### 3.1 Comparison between observed and CRU rainfall datasets

The variations in monthly and annual rainfall over eastern China based on both the observed stations and CRU gridded points from 1960 to 2015 are illustrated in Fig. 1. The monthly mean precipitation is shown in dashed lines and the climatological average is depicted in solid red lines (Fig. 1a, b). It can be seen in Fig. 1 that the climatological variability of observed rainfall along with months is quite similar to CRU gridded dataset. The slight discrepancy is that the annual mean rainfall is larger and smaller than 80 mm for CRU and observed datasets, respectively. The climatological rainfall is greater (lesser) than annual mean value from April to September (October to March), consistent with the periods of wet (dry) season (half year) selected in this study. These changes confirm that there is reasonable to categorize wet and dry seasons in conjunction with the variations in rainfall over eastern China. We further compare the time series of mean rainfall between observation and CRU datasets during wet and dry seasons (Fig. 1c, d), which suggest a strong level of similarity between observed and CRU datasets. High spatial similarity of the observed and CRU datasets during dry (Fig. 2a, c) and wet (Fig. 2b, d) seasons indicates that the spatial patterns from these two datasets are also consistent. In addition, the spectral analysis is also performed using the mean rainfall series of



the two datasets (not shown) and the similar results are also obtained. Those indicate that the rainfall variability for CRU dataset coincides with observations over eastern China. We use CRU dataset since it covers a much longer period and is therefore more suitable to examine the interdecadal variability. We present the following analyses in wet and dry seasons, respectively, to provide a concise result.

### 3.2 Dry season

The two leading PCs explain 34.22% and 13.44% of the total variance, they together capture around 50% variance. Fig. 3 depicts the time series of first PC that is flipped for convenient comparison, which is suggestive of a well correspond with the spatial mean rainfall. The first two eigenvectors, including spatial components and corresponding PCs, are shown in Fig. 4. The spatial pattern of the first eigenvector exhibits similar magnitudes and signs, indicating that the dominant pattern is coherent in eastern China, especially over southern China and coastal regions (Fig. 4a), this may be related to the propagation of the EAWM into mainland China. The second eigenvector displays a southeast-southwest dipole over southern China, this feature is coincident with the location and movement of the EASM (Ding et al., 2009). The time series of PCs also show considerable temporal changes with time, which are discussed in the spectral analysis.

Fig. 5 shows the correlation maps of climate variables and PC1 and PC2. Note that the signs of the PCs are flipped to ensure that the correlations are directly inferred as rainfall variability over eastern China. The correlation between PC1 and SSTs displays strong positive coefficients over the equatorial tropical Pacific and North



267 Pacific. While the negative connections are mainly found over the South China Sea  
 268 (SCS) and central-east Pacific, where it is featured by a La Niña SST pattern (Fig. 5a).  
 269 This indicates that when the eastern Pacific is colder as it is the case in La Niña  
 270 episodes, the strengthened convections may occur over southern China and adjacent  
 271 areas, leading to increased precipitation events, and vice versa in El Niño events. The  
 272 pattern of correlation with SLP is inconsistent with ones for SSTs, the significant  
 273 positive correlations are principally seen over the South Pacific and some tropical  
 274 regions immediate close to the Indian and Pacific oceans (Fig. 5b). Whereas, some  
 275 significant positive coefficients are located over the East China Sea, this may enhance  
 276 the southeastern wind anomalies that transport more water vapor fluxes into southern  
 277 China, providing conducive environmental backgrounds of forming more rainfall  
 278 events. Considering correlations with the geopotential heights at the 500 hPa (Fig. 5c),  
 279 the significant negative coefficients over the tropical central-east Pacific suggest a  
 280 weakened EAWM. When the EAWM weakens, the strengthened cold and dry air  
 281 intrudes into southern China and converges with warm and wet air from the oceans,  
 282 facilitating the occurrence of convective activities and heavy precipitation events  
 283 (Huang et al., 2018).

284 Correlation of SSTs with PC2 is reminiscent of the El Niño pattern, even though it  
 285 is not evident (Fig. 5d), an indication suggests that El Niño episode yields a dipole  
 286 pattern of the rainfall over southern China during dry season. The correlations with  
 287 SLP exhibiting positive coefficients are mainly distributed in the North Pacific and  
 288 Siberia, while the negative coefficients are principally situated over the equatorial



289 Pacific and Indian Oceans (Fig. 5e). Correlation coefficient between PC2 and 500 hPa  
 290 is relatively smaller and barely remarkable (Fig. 5f). Those imply that larger portion  
 291 of the variability induced by climate variables occurs in the first mode.

292 Compositing analyses of anomalous water vapor fluxes and divergence based on  
 293 highest 75th and lightest 25th percentile rainfall values, respectively, during dry  
 294 season are shown in Fig. 6. Considering the 25th percentile conditions, an anomalous  
 295 anticyclone is found over the WNP, while one branch of anomalous moisture fluxes to  
 296 the southern flank is transported eastward to eastern Pacific, meanwhile, another  
 297 branch is transported westward to Indian Ocean (Fig. 6a). As a result, the divergence  
 298 appears over eastern China, which is not suitable for the occurrence of precipitation  
 299 events. The adverse phenomena are found for the 75th percentile events (Fig. 6b). The  
 300 westward transportation of anomalous water vapor fluxes is prominent over the  
 301 equatorial Pacific, converging with the eastward transportation of moisture flux  
 302 anomalies from Indian Ocean over the SCS. Then the converged moisture fluxes are  
 303 transported northward, forming an anomalous cyclone over the WNP. The anomalous  
 304 water vapor fluxes over northern and western flanks of the WNP are transported into  
 305 eastern China, and anomalous terrestrial water vapor fluxes from Eurasia are also  
 306 transported into study domain. Those patterns provide favorable environmental  
 307 background and sufficient moisture supply for the formation of the convergence,  
 308 which is conducive to the occurrences of heavy rainfall events.

309 The wavelet coherence is performed on the PCs with large-scale ocean-atmosphere  
 310 circulation patterns to investigate the temporal variability of leading modes of rainfall



(Fig. 7). The local and global spectrums of PC1 indicate spectral peaks in the 1- to 4-year band and 6- to 10-year band further, which seems to be active during recent decades (Fig. 7a). For PC2, the 1- to 4-year band is active before the middle part of the twentieth century, while the 5- to 7-year band is concentrated in recent decades (Fig. 7b). ENSO index (Niño3.4) exhibits a significant peak of 2- to 7-year period and a relatively weaker peak of 8- to 16-year period (Fig. 7c). Fig. 7e displays that ENSO has a positive association with rainfall from 1900 to 1930, with a 4- to 8-year signal. There is also a positive relationship from 1980 to 2010, with an 1- to 6-year signal. These suggest that ENSO has a statistically positive impact on precipitation over eastern China in dry season. Wavelet filtering of the PC1 in the 4- to 8-year period with ENSO being coherent (Fig. 7c) is also made and illustrated in Fig. 3 as the solid line. PDO has a statistically positive connection with rainfall from 1940 to 1970, with a 7- to 8-year signal. While a negative association is seen from 1980 to 2000, with an 8- to 9-year signal (Fig. 7f). Particularly, the PDO is closely related to precipitation over eastern China.

### 3.3 Wet season

The total variance captured by first two PCs is about 30%, with PC1 and PC2 explaining 16.06% and 13.93%, respectively during wet season. These are smaller than total variances explained by two leading PCs of rainfall during dry season. The spatial mean precipitation is also captured by first PC (Fig. 8), which is flipped for easily comparing with spatial pattern. The solid line indicates the decadal smoother of first PC, and will be discussed later. While the low frequency of temporal variability



333 is seen in Fig. 8. The spatial components and corresponding PCs of first two  
 334 eigenvectors are shown in Fig. 9. A north-south dipole pattern is found for the first  
 335 eigenvector, with strong negative values located over southern China (Fig. 9a), which  
 336 has a close correlation with the variability of spatial mean precipitation (Fig. 8). This  
 337 rainfall pattern is also associated with the location and propagation of the EASM (Jin  
 338 et al., 2016). In wet season, the northward advance of the EASM circulations is  
 339 followed by three major rainy seasons sequentially: from May to mid-June, early  
 340 summer rainy season occurs in southern China. Then the mei-yu season presents over  
 341 the Yangtze-Huai river basins. The late summer rainy season ultimately forms over  
 342 northern China (Ding and Chan, 2005). Correspondingly, multiple synoptic and  
 343 climatological systems contribute to the occurrence of these rainfall events (Gao et al.,  
 344 2016; Luo et al., 2016). The second eigenvector exhibits the magnitudes of the  
 345 coherent signs in eastern China, with the peaks over the mid-lower reaches of YRB  
 346 (Fig. 9b). Moreover, the first two PCs display considerable temporal changes (Fig. 9c,  
 347 d) that are described in the discussion of spectral analysis.

348 The correlation map of PC1 with SSTs shows the strong positive coefficients over  
 349 the North Pacific and western tropical Pacific (Fig. 10a), while some statistically  
 350 negative correlations are distributed in the WNP. The positive correlations with SLP  
 351 exhibiting statistical significance are seen over the eastern Pacific, and the negative  
 352 values are found over the WNP and oceans to the eastern Australia (Fig. 10b). This is  
 353 roughly an opposite correlation pattern of SLP in comparison with dry season (Fig. 5b  
 354 and 10b). For 500 hPa, the positive correlations are mainly located over the WNP,



355 with positive values principally situated over the equatorial western Pacific, which are  
356 weaker as compared to the correlations in dry season. The correlation between SSTs  
357 and PC2 exhibits evident spatial features (Fig. 10d). Statistically significant negative  
358 coefficients are principally discovered over the eastern Pacific, reminiscent of the La  
359 Niña episode, this is suggestive of the La Niña telecommunication mechanisms  
360 responsible for the rainfall over eastern China during wet season. Note that  
361 statistically significant positive coefficients are mainly distributed over the northern  
362 Indian Ocean, resembling the Indian Ocean basin mode. To response the basin-wide  
363 warming of Indian Ocean, the strengthened convective heating in the tropical Indian  
364 Ocean will drive the Kelvin-wave-like eastern anomalies to the east. Then, the  
365 anticyclonic shear of the Kelvin-wave-like easterlies may drive the boundary layer  
366 divergence over the WNP by Ekman pumping, and therefore suppresses convection  
367 there. These suppressed convections simulate an anomalous anticyclone to the west.  
368 Ultimately, the anomalous anticyclone in the tropical WNP intensifies rainfall over  
369 eastern China (Li et al., 2017; Cao et al., 2020). The correlation of PC2 with SLP is  
370 much weaker compared to that of PC1, with significant negative coefficients located  
371 over far WNP (Fig. 10e). There also exists a weaker correlation with 500 hPa in  
372 comparison with PC1, and negative values mainly situate over the WNP (Fig. 10f).

373 Composited maps of moisture fluxes and divergence in high and light precipitation  
374 years during wet season are illustrated in Fig. 11. Unlike the anomalous changes in  
375 dry season (Fig. 6), the anomalous westward transportation of water vapor fluxes is  
376 found over the equatorial Pacific for the lightest 25th percentile precipitation events,



377 while the water vapor anomalies that are transported from Indian Ocean into eastern  
 378 China are not apparent (Fig. 11a). However, anomalous moisture fluxes are  
 379 transported northeastward passing eastern China, and fail to form convergence over  
 380 eastern China, which is not suitable for the occurrences of rainfall events. Fig. 11a  
 381 shows that eastern China is principally dominated by divergence during light rainfall  
 382 years. For the highest 75th percentile precipitation events, an anomalous cyclone  
 383 appears over the WNP, even though it is relatively weak (Fig. 11b). The water vapor  
 384 anomalies originated from WNP converge with those from Eurasia over eastern China,  
 385 as illustrated in Fig. 11b. Most of the eastern China is dominated by convergence,  
 386 providing inductive environmental backgrounds of the occurrences of heavy rainfall  
 387 events. In addition, the anticyclone and cyclone are seen over the Indian Ocean during  
 388 light and high rainfall years, respectively, which is generally consistent with the  
 389 Indian Ocean capacitor effects on the Indo–western Pacific climate in summer (Xie et  
 390 al., 2009).

391 The local and global spectrum of PC1 suggests the spectral peaks in the 1- to 5-year  
 392 and 6- to 10-year bands, as well as 16- to 32-year band further, these periods are  
 393 likely more active during recent decades (Fig. 12a). On the other hand, the PC2 shows  
 394 2- to 5-year and 5- to 8-year bands, as well as 16- to 24-year band. The first period  
 395 seems to be active in recent decades, and second and third periods are active from  
 396 1920 to 1980 (Fig. 12b). The ENSO index exhibits remarkable peaks of the 3- to  
 397 7-year period, which is active after 1950s (Fig. 12c). ENSO events have a statistically  
 398 negative relationship with rainfall over eastern China in wet season, with a 4- to



399 8-year signal, while other signals are not evident enough, even though they occur  
 400 intermittently during the entire twentieth century (Fig. 12e). These suggest that the  
 401 modulation of ENSO on wet season precipitation is mainly concentrated at the  
 402 interannual scale, consistent with those in dry season. This also coincides with the  
 403 interannual band of the wavelet filtering of the PC1 (Fig. 8). Fig. 12f shows that PDO  
 404 events have statistically significant positive associations with wet season rainfall from  
 405 1920 to 1940, with a 9- to 15-year signal. The significant negative connection with  
 406 rainfall exhibits a 4- to 7-year signal from 1930 to 1950. It can be seen from Fig. 7f  
 407 and Fig. 12f that PDO events have a stronger influence on rainfall in wet season than  
 408 that in dry season.

409 The changing connections between leading modes of precipitation and large-scale  
 410 modes of climate variability with time are accessed by BDLM (Fig. 13). We display  
 411 the results that have discernable changes along with time, and ignore the results  
 412 without discernable variations. The intercept from BDLM of PC1 and ENSO exhibits  
 413 a slight increase from 1920 to 1960, then turns into a decrease condition and  
 414 experiences zero value around the 1980s (Fig. 13a), suggesting that ENSO triggers a  
 415 negative (positive) impact before (after) the 1980s, and the influences of ENSO  
 416 become strengthened during recent decades. The intercept of PC2 and ENSO shows  
 417 negative values, and is gradually decreasing with time, which indicates that the  
 418 impacts of ENSO on PC2 are weakening during the entire century (Fig. 13b).  
 419 Considering the effects of PDO, the positive connection between PDO and PC1  
 420 exhibits a decrease until 1980s, then the impacts of PDO on rainfall over eastern



China are strengthening in recent decades (Fig. 13c). However, almost the opposite phenomenon is found for the connection between PC2 and PDO (Fig. 13d). The negative intercept is getting close to zero with time before 1980s, suggesting that the impact of PDO on PC1 is decreasing during this period. Then the positive connection of PC2 and PDO become strengthened after 2000s, indicating that the effect of PDO on PC2 is enhanced after this period. These results are important applications on the predictability of the rainfall events over eastern China based on the ENSO and PDO (Gao et al., 2017), since the ENSO and PDO has impacted the predictability of early summer monsoon precipitation in south China with the changes in connections between climate variability modes and rainfall (Chan and Zhou, 2005).

#### 4. Discussion and conclusions

Space-time variability of rainfall during dry and wet seasons over eastern China is examined by utilizing PCA, wavelet coherence and BDLM, based on the CRU gridded and observed rainfall datasets. In the overlapping period of 1960-2015, these two rainfall datasets are consistent in their temporal and spatial patterns in both seasons over eastern China. While the CRU gridded data has a much longer period (1901-2016) and is more suitable to analyze the interdecadal variability of rainfall.

The PCs exhibit notably temporal changes at the interannual and interdecadal scales. In dry season, the first and second eigenvectors account for 34.2% and 13.4% of variance, they exhibit coherent and dipole patterns of rainfall over southeastern China and southern China, respectively, which are generally coincident with the shifts of ENSO phases. Particularly, the strengthened rainfall over southeastern China is



443 associated with the La Niña episodes, and the dipole pattern of precipitation in  
444 southern China occurs during El Niño years. Moreover, the variations in rainfall over  
445 eastern China during dry season are also affected by the intensity of EAWM and the  
446 patterns of SLP. In wet season, first and second eigenvectors show dipole and  
447 coherence of rainfall patterns, respectively, which are roughly contrary to that in dry  
448 season. And the two leading PCs account for 16.1% and 13.9% of variance,  
449 respectively. The circulations responsible for the changes in rainfall over eastern  
450 China are also generally opposite to those during dry season.

451 Composited analyses illustrate the southeastward and southwestward  
452 transportations of moisture flux anomalies from southern portion of eastern China,  
453 and there is no convergence occurred over study region for 25th percentile rainfall  
454 events during dry season. In the years with highest (75th percentile) rainfall events,  
455 the anomalous moisture fluxes from equatorial Pacific and Indian Ocean are  
456 transported into eastern China through SCS, leading to the convergence with the  
457 anomalous water vapor fluxes from WNP and Eurasia in eastern China, providing  
458 sufficient moisture supply and environmental backgrounds for the occurrences of  
459 precipitation events. In wet season, the anomalous variations in moisture fluxes are  
460 different with that during dry season. For the lightest rainfall years, the water vapor  
461 anomalies that are transported from equatorial Pacific pass through eastern China, this  
462 northeastward transportation of water vapor anomalies fails to form a convergence in  
463 study region. Thus, most of the eastern China is consequently dominated by the  
464 divergence. However, the opposite phenomena are found for the 75th percentile



465 events, the water vapor anomalies from WNP converge with the anomalous moisture  
466 fluxes from Eurasia, they are transported southwestward into eastern China, resulting  
467 in heavy precipitation events. Note that the anticyclone and cyclone in Indian Ocean  
468 also play an important role to the occurrences of rainfall events over eastern China in  
469 addition to the forcing factors originated from Pacific Ocean (Xie et al., 2009; Li et al.,  
470 2017).

471 ENSO has a statistically positive (negative) association with rainfall during dry  
472 (wet) season in eastern China, with a 4- to 8-year signal. The impacts of ENSO on  
473 rainfall are principally concentrated at the interannual scale in both dry and wet  
474 seasons. PDO has a statistically positive (negative) relationship with rainfall in both  
475 seasons, exhibiting a 7- to 8-year (8- to 9-year) signal in dry season. And the  
476 statistically significant positive (negative) associations between PDO and  
477 precipitation over eastern China is seen with 9- to 15-year (4- to 7-year) signal. In  
478 short, the effects of PDO on rainfall show multiple time scales compared to these of  
479 ENSO. Moreover, the PDO triggers a stronger impact on precipitation over eastern  
480 China in wet season than dry season. Previous studies have revealed that PDO has a  
481 significant effect on the movement of rainbelt over eastern China during the rainy  
482 seasons, which influence the spatial distribution of rainfall events (i.e., southern flood  
483 and northern drought) (Li et al., 2010; Gao et al., 2017). Our findings further confirm  
484 those phenomena in eastern China at the interdecadal scale.

485 The analyses using BDLM suggest that there exists no significant time-varying  
486 relationship between large-scale modes of climate variability and rainfall over eastern



487 China in dry season. In wet season, the intercept of ENSO and PC2 gradually  
488 decreases with time, suggesting that the influences of ENSO on PC2 are gradually  
489 weakening in the entire century. The effect of PDO on PC1 is decreasing before 1980s,  
490 then shifts into positive connection after 2000s. The insights of spatiotemporal  
491 variability of rainfall over eastern China at different time scales, and the temporal  
492 variability of the strengths between climate variability modes (ENSO and PDO) and  
493 rainfall will be of great importance for developing skillful precipitation forecasting  
494 model. Moreover, BDLM provides a flexible regression method to incorporate the  
495 predictors with varying strengths, the model parameters are therefore estimated  
496 dynamically at each time, which enable to capture the time-varying predictors. The  
497 results in this study can also be adopted to develop seasonal precipitation forecasting  
498 models. Particularly, the asymmetry of the rainfall over eastern China and ENSO  
499 teleconnections in dry and wet seasons indicate the different underlying causes during  
500 El Niño and La Niña episodes, which can potentially improve the forecasting skills,  
501 these phenomena are also true for different phases of PDO episodes. The physical and  
502 human infrastructures over eastern China have suffered from severe floods and  
503 droughts, therefore, the skillful hydroclimate projections of space–time variability of  
504 rainfall will facilitate policy makers to develop the effective mitigation strategies.

505

506



507 **Author contributions.**

508 Gao T and Cao F designed all the experiments. Gao T and Cao F conducted all the  
509 experiments and analyzed the results. All the authors contributed to the preparation of  
510 the English editing.

511

512 **Competing interests.**

513 The authors declare that they have no conflict of interest.

514

515 **Acknowledgments**

516 This study is jointly supported by Natural Science Foundation and Sci-tech  
517 development project of Shandong Province (No. ZR2018MD014; J18KA210), Key  
518 research and development plan of Shandong province in 2019 (No. 2019GGX105021),  
519 Project funded by China Postdoctoral Science Foundation (No. 119100582H;  
520 1191005830), and Project of National Natural Science Foundation of China (No.  
521 41630532).

522



523

## 524 **References**

- 525 Bao, C.-L.: Synoptic Meteorology in China. China Ocean Press, 209 pp, 1987.
- 526 Cao, F., Gao, T., Dan, L., Ma, Z., Chen, X., Zou, L., and Zhang, L.: Synoptic-scale atmospheric  
 527 circulation anomalies associated with summertime daily precipitation extremes in the middle – lower  
 528 reaches of the Yangtze River Basin, *Clim Dynam*, 53, 3109-3129,  
 529 <https://doi.org/10.1007/s00382-019-04687-3>, 2020.
- 530 Chan, J. C., and Zhou, W.: PDO, ENSO and the early summer monsoon rainfall over south China,  
 531 *Geophys Res Lett*, 32, L08810, <https://doi.org/10.1029/2004GL022015>, 2005.
- 532 Chang, C. P., Zhang, Y., and Li, T.: Interannual and interdecadal variations of the East Asian summer  
 533 monsoon and tropical Pacific SSTs. Part I: Roles of the subtropical ridge, *J Climate*, 13, 4310-4325,  
 534 [https://doi.org/10.1175/1520-0442\(2000\)013<4326:IAIVOT>2.0.CO;2](https://doi.org/10.1175/1520-0442(2000)013<4326:IAIVOT>2.0.CO;2), 2000a.
- 535 Chang, C. P., Zhang, Y., and Li, T.: Interannual and interdecadal variations of the East Asian summer  
 536 monsoon and tropical Pacific SSTs. Part II: Meridional structure of the monsoon, *J Climate*, 13,  
 537 4326-4340, [https://doi.org/10.1175/1520-0442\(2000\)013<4326:IAIVOT>2.0.CO;2](https://doi.org/10.1175/1520-0442(2000)013<4326:IAIVOT>2.0.CO;2), 2000b.
- 538 Chen, S., Zhu, Z., Ge, Z., Kang, Z., and He, J.: The diversity of La Niña decay and the corresponding  
 539 spring and summer precipitation anomalies over eastern China, *Int J Climatol*, 11,  
 540 <https://doi.org/10.1002/joc.6100>, 2019.
- 541 Chen, W., Feng, J., and Wu, R.: Roles of ENSO and PDO in the link of the East Asian winter monsoon  
 542 to the following summer monsoon, *J Climate*, 26, 622-635,  
 543 <https://doi.org/10.1175/JCLI-D-12-00021.1>, 2013.
- 544 Coulibaly, P., and Burn, D. H.: Spatial and temporal variability of Canadian seasonal streamflows, *J*



- 545 *Climate*, 18, 191-210, <https://doi.org/10.1175/JCLI-3258.1>, 2005.
- 546 Domroes, M., and G. Peng: The Climate of China. SpringerVerlag, 361 pp, 1988.
- 547 Ding, Y. H., and Chan, J. C.: The East Asian summer monsoon: an overview, *Meteorol Atmos Phys*, 89,
- 548 117-142, <https://doi.org/10.1007/s00703-005-0125-z>, 2005.
- 549 Ding, Y., Sun, Y., Wang, Z., Zhu, Y., and Song, Y.: Inter - decadal variation of the summer
- 550 precipitation in China and its association with decreasing Asian summer monsoon Part II: Possible
- 551 causes, *Int J Climatol*, 29, 1926-1944, <https://doi.org/10.1002/joc.1615>, 2009.
- 552 Gao, T., Wang, H. J., and Zhou, T.: Changes of extreme precipitation and nonlinear influence of
- 553 climate variables over monsoon region in China, *Atmos Res*, 197, 379-389,
- 554 <http://dx.doi.org/10.1016/j.atmosres.2017.07.017>, 2017.
- 555 Gao, T., Xie, L., and Liu, B.: Association of extreme precipitation over the Yangtze River Basin with
- 556 global air - sea heat fluxes and moisture transport, *Int J Climatol*, 36, 3020-3038,
- 557 <https://doi.org/10.1002/joc.4534>, 2016.
- 558 Gao, T., and Wang, H.: Trends in precipitation extremes over the Yellow River basin in North China:
- 559 Changing properties and causes, *Hydrol Process*, 31, 2412-2428, <https://doi.org/10.1002/hyp.11192>,
- 560 2017.
- 561 Ge, J., You, Q., and Zhang, Y.: Effect of Tibetan Plateau heating on summer extreme precipitation in
- 562 eastern China, *Atmos Res*, 218, 364-371, <https://doi.org/10.1016/j.atmosres.2018.12.018>, 2019.
- 563 Grinsted, A., Moore, J. C., and Jevrejeva, S.: Application of the cross wavelet transform and wavelet
- 564 coherence to geophysical time series, *Nonlinear Proc Geoph*, 11, 561-566,
- 565 <https://doi.org/10.5194/npg-11-561-2004>, 2004.
- 566 Hannachi, A., Jolliffe, I. T., and Stephenson, D. B.: Empirical orthogonal functions and related



567 techniques in atmospheric science: A review, *Int J Climatol*, 27, 1119-1152,  
 568 <https://doi.org/10.1002/joc.1499>, 2007.

569 Harris, I., Jones, P. D., Osborn, T. J., and Lister, D. H.: Updated high - resolution grids of monthly  
 570 climatic observations - the CRU TS3. 10 Dataset, *Int J Climatol*, 34, 623-642,  
 571 <https://doi.org/10.1002/joc.3711>, 2014.

572 He, C., Lin, A., Gu, D., Li, C., Zheng, B., and Zhou, T.: Interannual variability of Eastern China  
 573 Summer Rainfall: the origins of the meridional triple and dipole modes, *Clim Dynam*, 48, 683-696,  
 574 <https://doi.org/10.1007/s00382-016-3103-x>, 2017.

575 Hu, C., Chen, D., Huang, G., and Yang, S.: Dipole Types of Autumn Precipitation Variability Over the  
 576 Subtropical East Asia - Western Pacific Modulated by Shifting ENSO, *Geophys Res Lett*, 45,  
 577 9123-9130, <https://doi.org/10.1029/2018GL078982>, 2018.

578 Huang, D., Dai, A., Zhu, J., Zhang, Y., and Kuang, X.: Recent Winter Precipitation Changes over  
 579 Eastern China in Different Warming Periods and the Associated East Asian Jets and Oceanic  
 580 Conditions, *J Climate*, 30, 4443-4462, <https://journals.ametsoc.org/doi/10.1175/JCLI-D-16-0517.1>,  
 581 2017.

582 Huang, R., and Sun, F.: Impacts of the tropical western Pacific on the East Asian summer monsoon,  
 583 *Journal of the Meteorological Society of Japan. Ser. II*, 70, 243-256,  
 584 <http://dx.doi.org/10.3878/j.issn.1006-9895.2006.06.01>, 1992.

585 Huang, R., and Wu, Y.: The influence of ENSO on the summer climate change in China and its  
 586 mechanism, *Adv Atmos Sci*, 6, 21-32, <https://doi.org/10.1007/BF02656915>, 1989.

587 Huang, W., He, X., Yang, Z., Qiu, T., Wright, J. S., Wang, B., and Lin, D.: Moisture sources for  
 588 wintertime extreme precipitation events over South China during 1979 - 2013, *Journal of*



- 589 *Geophysical Research: Atmospheres*, 123, 6690-6712, <https://doi.org/10.1029/2018JD028485>, 2018.
- 590 Jin, D., Hameed, S. N., and Huo, L.: Recent changes in ENSO teleconnection over the western Pacific
- 591 impacts the eastern China precipitation dipole, *J Climate*, 29, 7587-7598,
- 592 <https://doi.org/10.1175/JCLI-D-16-0235.1>, 2016.
- 593 Kalnay, E., Kanamitsu, M., Kistler, R., Collins, W., Deaven, D., Gandin, L., Iredell, M., Saha, S.,
- 594 White, G., and Woollen, J.: The NCEP/NCAR 40-year reanalysis project, *B Am Meteorol Soc*, 77,
- 595 437-471, [https://doi.org/10.1175/1520-0477\(1996\)077<0437:TNYRP>2.0.CO;2](https://doi.org/10.1175/1520-0477(1996)077<0437:TNYRP>2.0.CO;2), 1996.
- 596 Krishnaswamy, J., Vaidyanathan, S., Rajagopalan, B., Bonell, M., Sankaran, M., Bhalla, R. S., and
- 597 Badiger, S.: Non-stationary and non-linear influence of ENSO and Indian Ocean Dipole on the
- 598 variability of Indian monsoon rainfall and extreme rain events, *Clim Dynam*, 45, 175-184,
- 599 <https://doi.org/10.1007/s00382-014-2288-0>, 2015.
- 600 Lei, Y. U.: Potential correlation between the decadal East Asian summer monsoon variability and the
- 601 Pacific decadal oscillation, *Atmospheric and Oceanic Science Letters*, 6, 394-397,
- 602 <https://doi.org/10.3878/j.issn.1674-2834.13.0040>, 2013.
- 603 Li, H., Dai, A., Zhou, T., and Lu, J.: Responses of East Asian summer monsoon to historical SST and
- 604 atmospheric forcing during 1950 - 2000, *Clim Dynam*, 34, 501-514,
- 605 <https://doi.org/10.1007/s00382-008-0482-7>, 2010.
- 606 Li, Y., Ma, B., Feng, J., and Lu, Y.: Influence of the strongest central Pacific El Niño - Southern
- 607 Oscillation events on the precipitation in eastern China, *Int J Climatol*, 39, 3076-3090,
- 608 <https://doi.org/10.1002/joc.6004>, 2019.
- 609 Li, T., Bin, W., Bo, W. U., Tianjun, Z., and Chih-Pei Chang, R. Z.: Theories on Formation of an
- 610 Anomalous Anticyclone in Western North Pacific during El Niño: A Review, *Journal of*



- 611 *Meteorological Research*, 31, 987-1006, <https://doi.org/10.1007/s13351-017-7147-6>, 2017.
- 612 Liu, J., Wang, H., Lu, E., and Kumar, A.: Decadal modulation of East China winter precipitation by
- 613 ENSO, *Clim Dynam*, 1-15, <https://doi.org/10.1007/s00382-016-3427-6>, 2016.
- 614 Liu, R., Liu, S. C., Cicerone, R. J., Shiu, C., Li, J., Wang, J., and Zhang, Y.: Trends of extreme
- 615 precipitation in eastern China and their possible causes, *Adv Atmos Sci*, 32, 1027-1037,
- 616 <https://doi.org/10.1007/s00376-015-5002-1>, 2015.
- 617 Luo, M., and Lau, N. C.: Increasing heat stress in urban areas of eastern China: Acceleration by
- 618 urbanization, *Geophys Res Lett*, 45, 13-60, <https://doi.org/10.3390/su11123413>, 2018.
- 619 Luo, Y., Wu, M., Ren, F., Li, J., and Wong, W.: Synoptic situations of extreme hourly precipitation
- 620 over China, *J Climate*, 29, 8703-8719, <https://doi.org/10.1175/JCLI-D-16-0057.1>, 2016.
- 621 Ma, Z.: The interdecadal trend and shift of dry/wet over the central part of North China and their
- 622 relationship to the Pacific Decadal Oscillation (PDO), *Chinese Sci Bull*, 52, 2130-2139,
- 623 <https://doi.org/10.1007/s11434-007-0284-z>, 2017.
- 624 Qian, C., and Zhou, T.: Multidecadal variability of North China aridity and its relationship to PDO
- 625 during 1900 – 2010, *J Climate*, 27, 1210-1222, <https://doi.org/10.1175/JCLI-D-13-00235.1>, 2014.
- 626 Rajagopalan, B., and Zagana, E.: Space-time variability of Indonesian rainfall at inter-annual and
- 627 multi-decadal time scales, *Clim Dynam*, 47, 2975-2989,
- 628 <http://dx.doi.org/10.1007/s00382-016-3008-8>, 2016.
- 629 Rayner, N. A., Parker, D. E., Horton, E. B., Folland, C. K., Alexander, L. V., Rowell, D. P., Kent, E. C.,
- 630 and Kaplan, A.: Global analyses of sea surface temperature, sea ice, and night marine air temperature
- 631 since the late nineteenth century, *Journal of Geophysical Research: Atmospheres*, 108.4407,
- 632 <https://doi.org/10.1029/2002JD002670>, 2003.



- 633 Sun, Q., Miao, C., Qiao, Y., and Duan, Q.: The nonstationary impact of local temperature changes and  
 634 ENSO on extreme precipitation at the global scale, *Clim Dynam*, 49, 4281-4292,  
 635 <https://doi.org/10.1007/s00382-017-3586-0>, 2017.
- 636 Torrence, C., and Webster, P. J.: Interdecadal changes in the ENSO–monsoon system, *J Climate*, 12,  
 637 2679-2690, [https://doi.org/10.1175/1520-0442\(1999\)012<2679:ICITEM>2.0.CO;2](https://doi.org/10.1175/1520-0442(1999)012<2679:ICITEM>2.0.CO;2), 1999.
- 638 Wang, B., Liu, J., Kim, H., Webster, P. J., Yim, S., and Xiang, B.: Northern Hemisphere summer  
 639 monsoon intensified by mega-El Niño/southern oscillation and Atlantic multidecadal oscillation,  
 640 *Proceedings of the National Academy of Sciences*, 110, 5347-5352,  
 641 <https://doi.org/10.1073/pnas.1219405110>, 2013.
- 642 Wang, B., Wu, R., and Fu, X.: Pacific-East Asian teleconnection: how does ENSO affect East Asian  
 643 climate? *J Climate*, 13, 1517-1536,  
 644 [https://doi.org/10.1175/1520-0442\(2000\)013<1517:PEATHD>2.0.CO;2](https://doi.org/10.1175/1520-0442(2000)013<1517:PEATHD>2.0.CO;2), 2000.
- 645 Wang, L., Chen, W., and Huang, R.: Interdecadal modulation of PDO on the impact of ENSO on the  
 646 East Asian winter monsoon, *Geophys Res Lett*, 35, doi: 10.1029/2008GL035287,  
 647 <https://doi.org/10.1029/2008GL035287>, 2008.
- 648 Wang, Y., and Zhou, L.: Observed trends in extreme precipitation events in China during 1961 – 2001  
 649 and the associated changes in large-scale circulation, *Geophys. Res. Lett*, 32, L9707,  
 650 <https://doi.org/10.1029/2005GL022574>, 2005.
- 651 Webster, P. J., Magana, V. O., Palmer, T. N., Shukla, J., Tomas, R. A., Yanai, M., and Yasunari, T.:  
 652 Monsoons: Processes, predictability, and the prospects for prediction, *Journal of Geophysical*  
 653 *Research: Oceans*, 103, 14451-14510, <https://doi.org/10.1029/97JC02719>, 1998.
- 654 Wu, R., Hu, Z., and Kirtman, B. P.: Evolution of ENSO-related rainfall anomalies in East Asia, *J*



- 655 *Climate*, 16, 3742-3758, [https://doi.org/10.1175/1520-0442\(2003\)016<3742:EOERAI>2.0.CO;2](https://doi.org/10.1175/1520-0442(2003)016<3742:EOERAI>2.0.CO;2),  
 656 2003.
- 657 Xie, S., Hu, K., Hafner, J., Tokinaga, H., Du, Y., Huang, G., and Sampe, T.: Indian Ocean capacitor  
 658 effect on Indo-western Pacific climate during the summer following El Niño, *J Climate*, 22, 730-747,  
 659 <https://doi.org/10.1175/2008JCLI2544.1>, 2009.
- 660 Xu, K., Yang, D., Yang, H., Li, Z., Qin, Y., and Shen, Y.: Spatio-temporal variation of drought in  
 661 China during 1961 - 2012: A climatic perspective, *J Hydrol*, 526, 253-264,  
 662 <https://doi.org/10.1016/j.jhydrol.2014.09.047>, 2015.
- 663 Yang, F., and Lau, K. M.: Trend and variability of China precipitation in spring and summer: linkage to  
 664 sea - surface temperatures, *Int J Climatol*, 24, 1625-1644, <https://doi.org/10.1002/joc.1094>, 2004.
- 665 Yang, Q., Ma, Z., Fan, X., Yang, Z., Xu, Z., and Wu, P.: Decadal Modulation of Precipitation Patterns  
 666 over Eastern China by Sea Surface Temperature Anomalies, *J Climate*, 30, 7017-7033,  
 667 <https://doi.org/10.1175/JCLI-D-16-0793.1>, 2017.
- 668 Yang, Q., Ma, Z., and Xu, B.: Modulation of monthly precipitation patterns over East China by the  
 669 Pacific Decadal Oscillation, *Climatic Change*, 144, 405-417,  
 670 <https://doi.org/10.1007/s10584-016-1662-9>, 2017.
- 671 Yu, L., Furevik, T., Otterå O. H., and Gao, Y.: Modulation of the Pacific Decadal Oscillation on the  
 672 summer precipitation over East China: a comparison of observations to 600-years control run of  
 673 Bergen Climate Model, *Clim Dynam*, 44, 475-494, <https://doi.org/10.1007/s00382-014-2141-5>,  
 674 2015.
- 675 Zhai, P., Zhang, X., Wan, H., and Pan, X.: Trends in total precipitation and frequency of daily  
 676 precipitation extremes over China, *J Climate*, 18, 1096-1108, <https://doi.org/10.1175/JCLI-3318.1>,



2005.

Zhang, L., and Zhou, T.: Drought over East Asia: a review, *J Climate*, 28, 3375-3399,  
<https://doi.org/10.1175/JCLI-D-14-00259.1>, 2015.

Zhang, R., Sumi, A., and Kimoto, M.: Impact of El Niño on the east Asian monsoon: A Diagnostic  
 Study of the '86/87 and '91/92 Events, *Journal of the Meteorological Society of Japan. Ser. II*, 74,  
 49-62, [https://doi.org/10.2151/jmsj1965.74.1\\_49](https://doi.org/10.2151/jmsj1965.74.1_49), 1996.

Zhu, Y., Wang, H., Ma, J., Wang, T., and Sun, J.: Contribution of the phase transition of Pacific  
 Decadal Oscillation to the late 1990s' shift in East China summer rainfall, *Journal of Geophysical  
 Research: Atmospheres*, 120, 8817-8827, <https://doi.org/10.1002/2015JD023545>, 2015.

Zhu, Y., Wang, H., Zhou, W., and Ma, J.: Recent changes in the summer precipitation pattern in East  
 China and the background circulation, *Clim Dynam*, 36, 1463-1473,  
<https://doi.org/10.1007/s00382-010-0852-9>, 2011.

Zhou T, Song F, Lin R, Chen X, Chen X.: Explaining extreme events of 2012 from a climate  
 perspective. *Bull Am Meteorol Soc*, 94:S1–S74, <https://doi.org/10.1175/BAMS-D-13-00085.1>, 2013.



# Figure captions

Figure 1. Annual climatological rainfall at all stations (STN) and grid (CRU) points shown as grey lines and their mean in a solid red line, (a) observation and (b) CRU. Seasonal mean precipitation anomalies from observation (black) and CRU (blue), (c) dry season and (d) wet season.

Figure 2. Spatial distribution of seasonal mean precipitation (mm/month) during 1960-2015 over eastern China from observation and CRU datasets, (a) and (c) are for dry season; (b) and (d) are for wet season.

Figure 3. Standardized time series of all dry season precipitation over eastern China as shown in red dashed line, the black dots denote flipped PC1 and the blue lines denote the decadal features of dry season precipitation.

Figure 4. (a) The first and (b) second EOFs for the rainfall in dry season. (c) The first and (d) second principal components (PCs) correspond to these EOFs from the rainfall in dry season. Both time series are normalized with respect to the corresponding standard deviations.

Figure 5. Correlation coefficients in dry season. (a) sea surface temperature and PC1, (b) mean sea level pressure with PC1, (c) geopotential height at the 500 hPa and PC1, (d) sea surface temperature and PC2, (e) mean sea level pressure with PC2 and (f) geopotential height at the 500 hPa with PC2. Hatching denotes the regions with statistical significance at the 95% confidence level. Black rectangle denotes the eastern China.

Figure 6. Vertically integrated water vapor anomalies (vector) and water vapor flux divergence (shading) composited from the lightest 25th (a) and highest 75th (b) percentile rainfall events in dry season. The water vapor flux unit is  $\text{kg m}^{-1} \text{s}^{-1}$  for and the water vapor flux divergence is  $\text{kg m}^{-2} \text{s}^{-1}$ . Green rectangle denotes the eastern China.

Figure 7. Wavelet spectra for dry season. (a) PC1, (b) PC2, (c) Niño3.4 index, (d) PDO index, (e) wavelet spectral coherence of PC1 and Niño3.4, and (f) wavelet spectral coherence of PC2 and PDO. The global spectra are shown on the right side of



722 the time varying wavelet spectra and, the black lines denote the statistical significance  
 723 at the 95% confidence level.

724 Figure 8. Standardized time series of all wet season precipitation over eastern China  
 725 as shown in red dashed line, the black dots denote flipped PC1 and the blue lines  
 726 denote the decadal features of wet season precipitation.

727 Figure 9. (a) The first and (b) second EOFs for the rainfall in wet season. (c) The first  
 728 and (d) second principal components (PCs) correspond to these EOFs from the  
 729 rainfall in wet season. Both time series are normalized with respect to the  
 730 corresponding standard deviations

731 Figure 10. Correlation coefficients in wet season. (a) sea surface temperature and PC1,  
 732 (b) mean sea level pressure with PC1, (c) geopotential height at the 500 hPa and PC1,  
 733 (c) sea surface temperature and PC2, (e) mean sea level pressure with PC2 and (f)  
 734 geopotential height at the 500 hPa with PC2. Hatching denotes the regions with  
 735 statistical significance at the 95% confidence level. Black rectangle denotes the  
 736 eastern China.

737 Figure 11. Vertically integrated water vapor anomalies (vector) and water vapor flux  
 738 divergence (shading) composited from the lightest 25th (a) and highest 75th (b)  
 739 percentile rainfall events in wet season. The water vapor flux unit is  $\text{kg m}^{-1} \text{s}^{-1}$  for and  
 740 the water vapor flux divergence is  $\text{kg m}^{-2} \text{s}^{-1}$ . Black rectangle denotes the eastern  
 741 China.

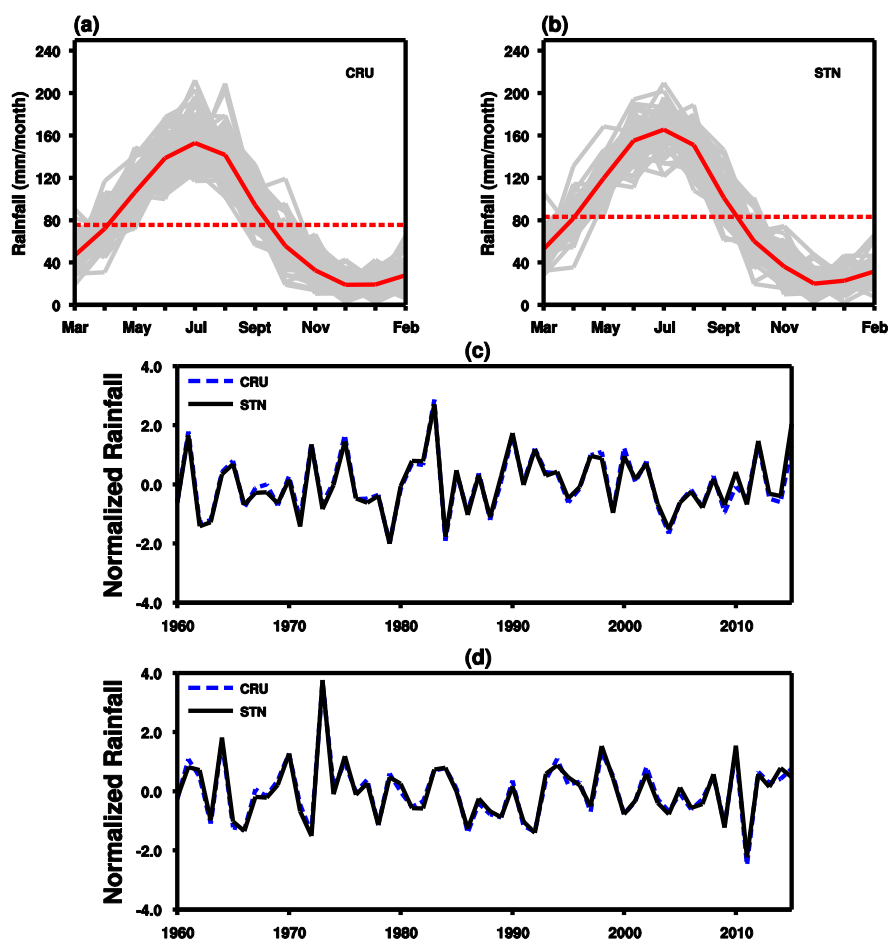
742 Figure 12. Wavelet spectra for wet season. (a) PC1, (b) PC2, (c) Niño3.4 index, (d)  
 743 PDO index, (e) wavelet spectral coherence of PC1 and Niño3.4, and (f) wavelet  
 744 spectral coherence of PC2 and PDO. The global spectra are shown on the right side of  
 745 the time varying wavelet spectra and, the black lines denote the statistical significance  
 746 at the 95% confidence level.

747 Figure 13. Changes in the relationships between rainfall and ENSO/PDO over time  
 748 during 1901-2015. Black solid lines denote the estimated time-varying slopes, along  
 749 with 25th and 75th percentile credible interval lines (red dotted lines) from the  
 750 Bayesian dynamic linear model analysis.

751



752



753

754 Figure 1. Annual climatological rainfall at all stations (STN) and grid (CRU) points

755 shown as grey lines and their mean in a solid red line, (a) observation and (b) CRU.

756 Seasonal mean precipitation anomalies from observation (black) and CRU (blue), (c)

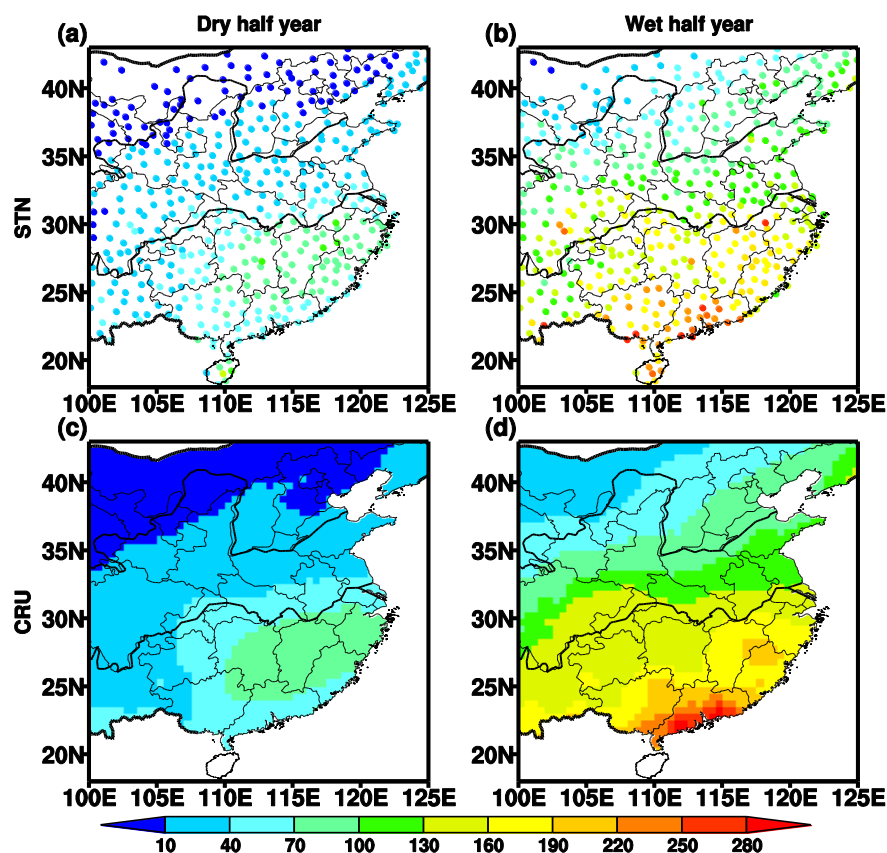
757 dry season and (d) wet season.

758

759



760



761

762 Figure 2. Spatial distribution of seasonal mean precipitation (mm/month) during

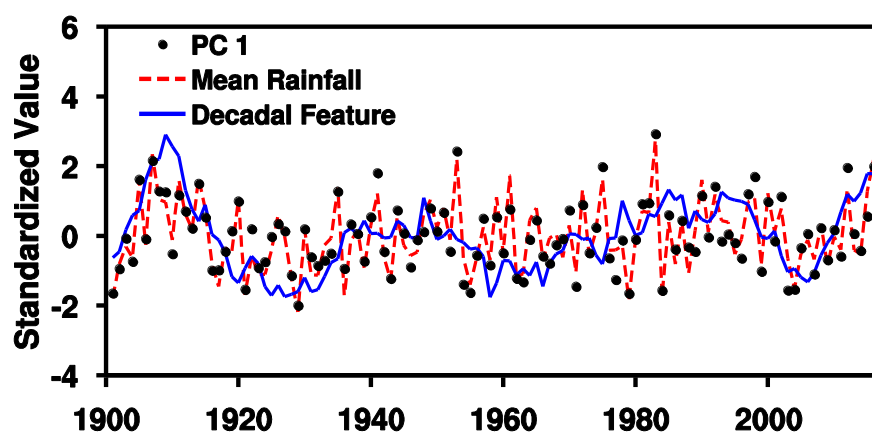
763 1960-2015 over eastern China from observation and CRU datasets, (a) and (c) are for

764 dry season; (b) and (d) are for wet season.

765



766



767

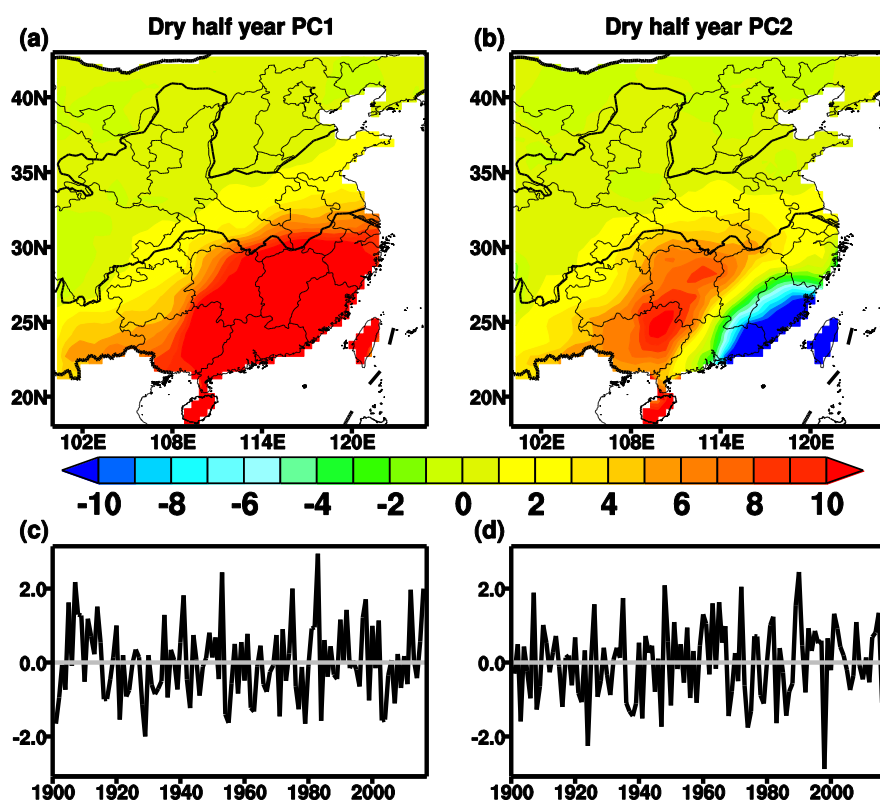
768 Figure 3. Standardized time series of all dry season precipitation over eastern China as  
 769 shown in red dashed line, the black dots denote flipped PC1 and the blue lines denote  
 770 the decadal features of dry season precipitation.

771

772



773



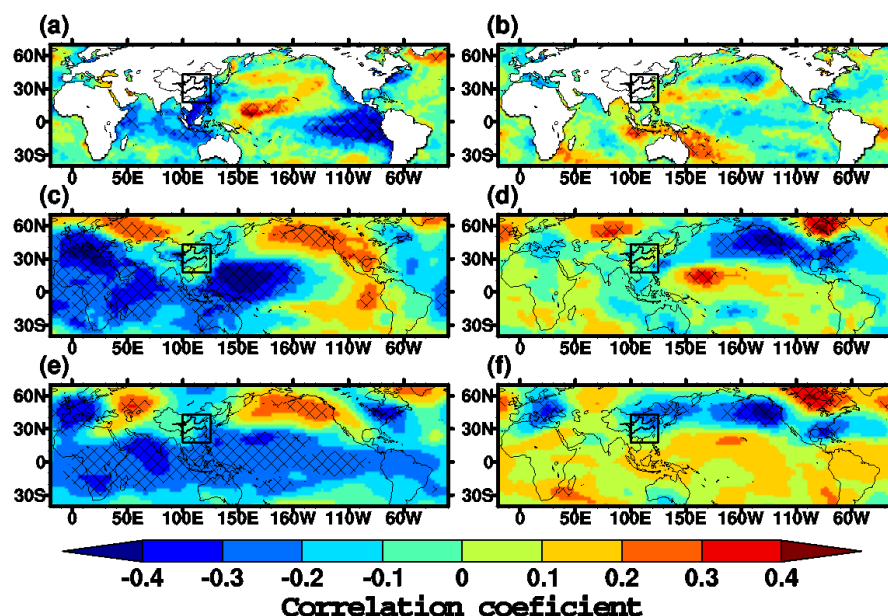
774

775 Figure 4. (a) The first and (b) second EOFs for the rainfall in dry season. (c) The first  
 776 and (d) second principal components (PCs) correspond to these EOFs from the  
 777 rainfall in dry season. Both time series are normalized with respect to the  
 778 corresponding standard deviations.

779

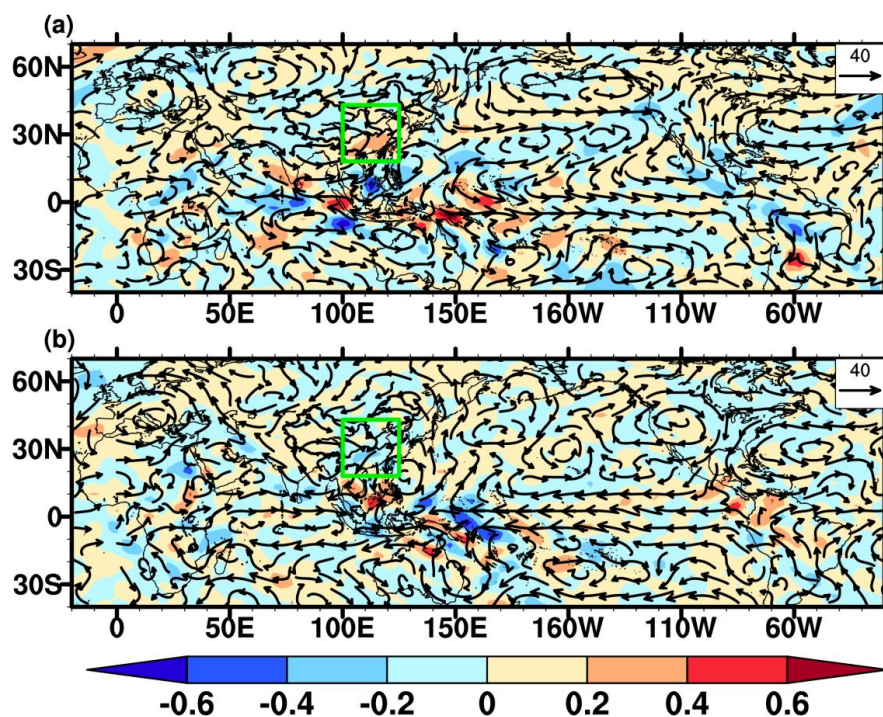


780



781

782 Figure 5. Correlation coefficients in dry season. (a) sea surface temperature and PC1,  
 783 (b) mean sea level pressure with PC1, (c) geopotential height at the 500 hPa and PC1,  
 784 (d) sea surface temperature and PC2, (e) mean sea level pressure with PC2 and (f)  
 785 geopotential height at the 500 hPa with PC2. Hatching denotes the regions with  
 786 statistical significance at the 95% confidence level. Black rectangle denotes the  
 787 eastern China.



788

789 Figure 6. Vertically integrated water vapor anomalies (vector) and water vapor flux  
 790 divergence (shading) composited from the lightest 25th (a) and highest 75th (b)  
 791 percentile rainfall events in dry season. The water vapor flux unit is  $\text{kg m}^{-1} \text{s}^{-1}$  for and  
 792 the water vapor flux divergence is  $\text{kg m}^{-2} \text{s}^{-1}$ . Green rectangle denotes the eastern  
 793 China.

794

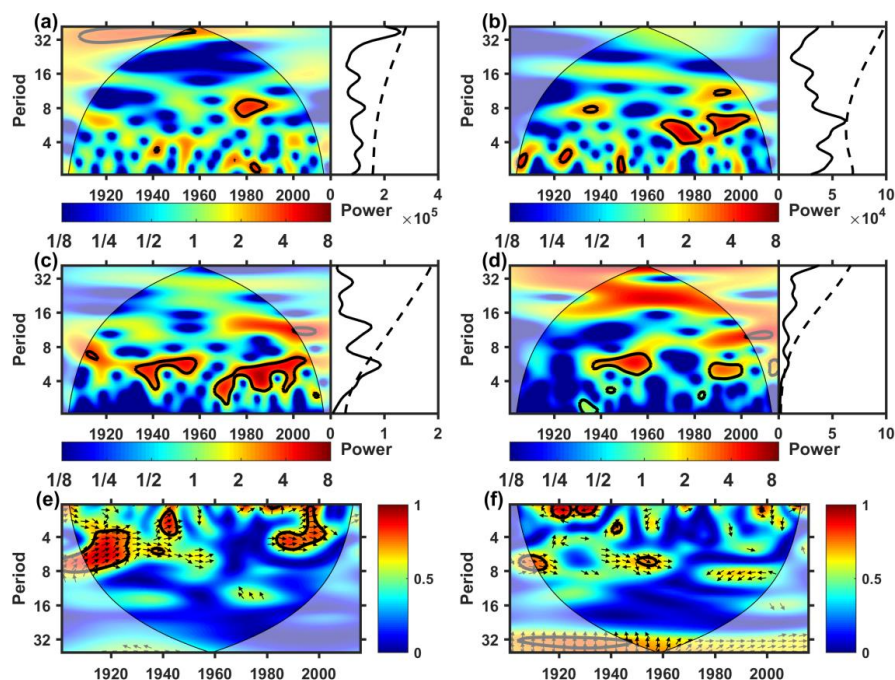
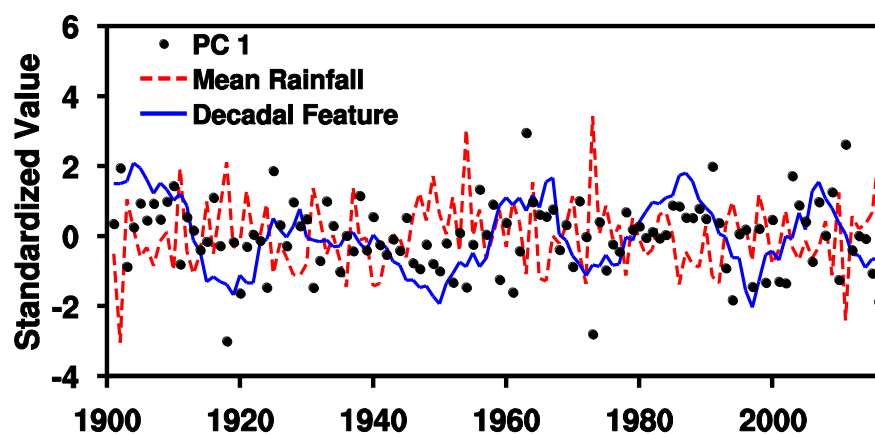


Figure 7. Wavelet spectra for dry season. (a) PC1, (b) PC2, (c) Niño3.4 index, (d) PDO index, (e) wavelet spectral coherence of PC1 and Niño3.4, and (f) wavelet spectral coherence of PC2 and PDO. The global spectra are shown on the right side of the time varying wavelet spectra and, the black lines denote the statistical significance at the 95% confidence level.



803



804

805 Figure 8. Standardized time series of all wet season precipitation over eastern China  
 806 as shown in red dashed line, the black dots denote flipped PC1 and the blue lines  
 807 denote the decadal features of wet season precipitation.

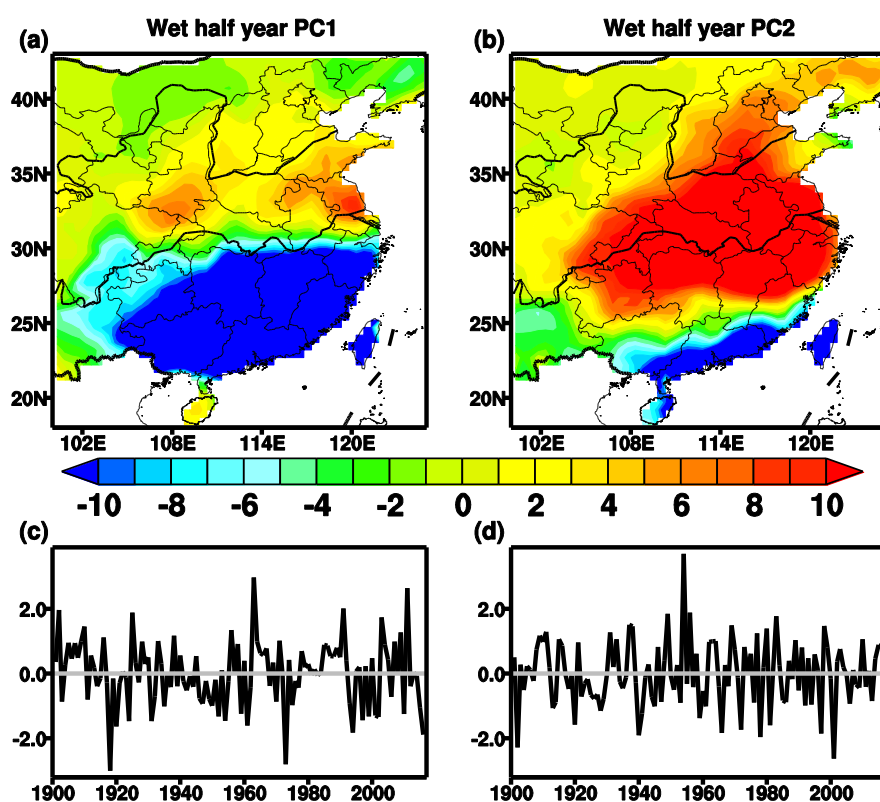
808

809

810



811



812

813 Figure 9. (a) The first and (b) second EOFs for the rainfall in wet season. (c) The first  
 814 and (d) second principal components (PCs) correspond to these EOFs from the  
 815 rainfall in wet season. Both time series are normalized with respect to the  
 816 corresponding standard deviations.

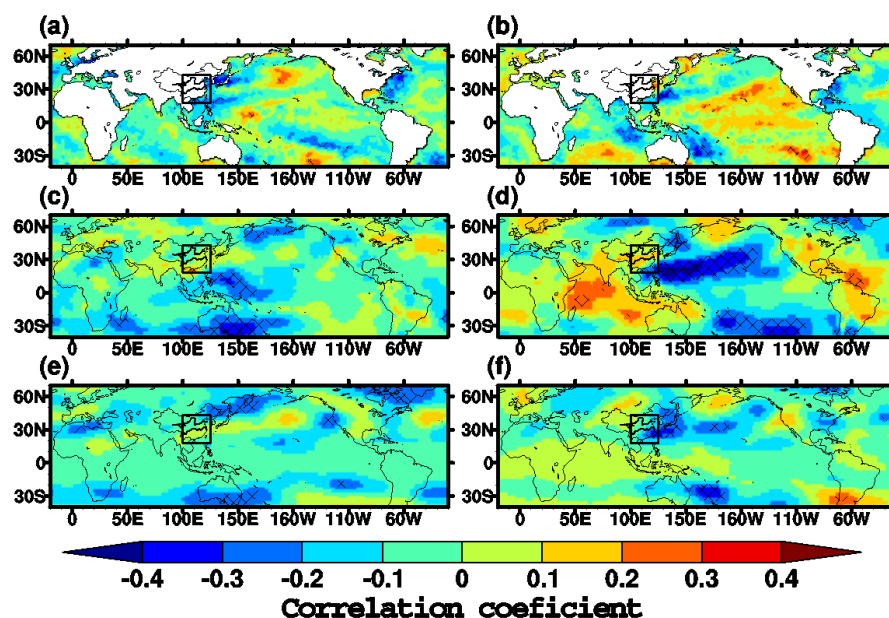
817

818

819



820

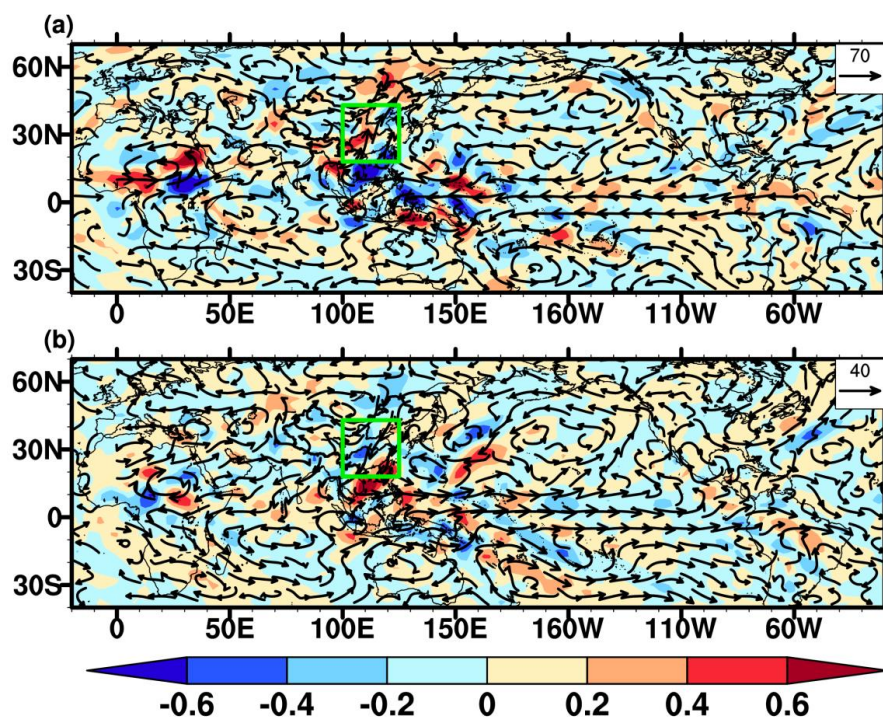


821

822 Figure 10. Correlation coefficients in wet season. (a) sea surface temperature and PC1,  
 823 (b) mean sea level pressure with PC1, (c) geopotential height at the 500 hPa and PC1,  
 824 (c) sea surface temperature and PC2, (e) mean sea level pressure with PC2 and (f)  
 825 geopotential height at the 500 hPa with PC2. Hatching denotes the regions with  
 826 statistical significance at the 95% confidence level. Black rectangle denotes the  
 827 eastern China.

828

829



830

831 Figure 11. Vertically integrated water vapor anomalies (vector) and water vapor flux  
 832 divergence (shading) composited from the lightest 25th (a) and highest 75th (b)  
 833 percentile rainfall events in wet season. The water vapor flux unit is  $\text{kg m}^{-1} \text{s}^{-1}$  for and  
 834 the water vapor flux divergence is  $\text{kg m}^{-2} \text{s}^{-1}$ . Green rectangle denotes the eastern  
 835 China.

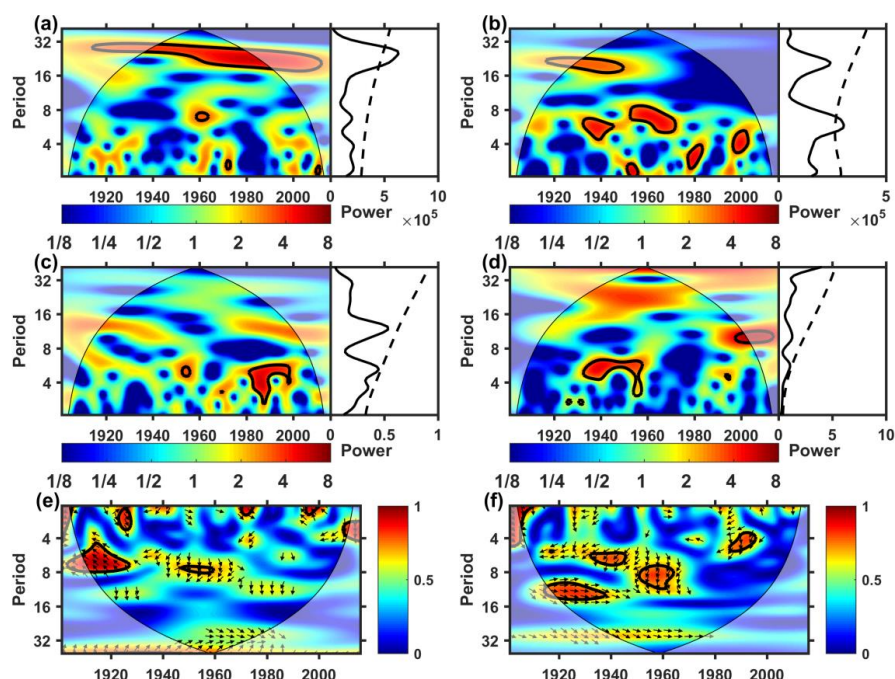
836

837

838



839



840

841 Figure 12. Wavelet spectra for wet season. (a) PC1, (b) PC2, (c) Niño3.4 index, (d)  
 842 PDO index, (e) wavelet spectral coherence of PC1 and Niño3.4, and (f) wavelet  
 843 spectral coherence of PC2 and PDO. The global spectra are shown on the right side of  
 844 the time varying wavelet spectra and, the black lines denote the statistical significance  
 845 at the 95% confidence level.

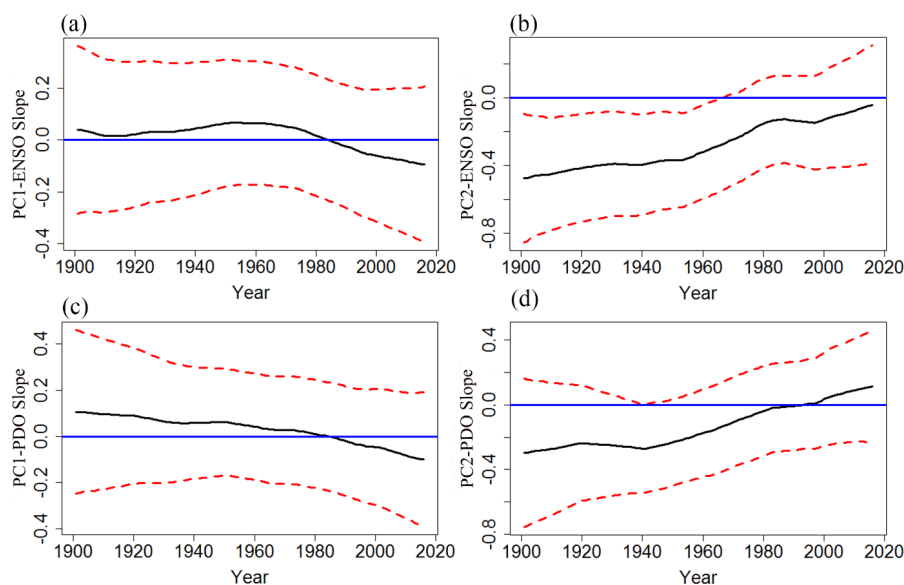
846

847

848



849



850

851 Figure 13. Changes in the relationships between rainfall and ENSO/PDO over time  
 852 during 1901-2015. Black solid lines denote the estimated time-varying slopes, along  
 853 with 25th and 75th percentile credible interval lines (red dashed lines) from the  
 854 Bayesian dynamic linear model analysis.

855

856